Petroleum Science 19 (2022) 2675–2682

Contents lists available at ScienceDirect

Petroleum Science

journal homepage: www.keaipublishing.com/en/journals/petroleum-science

Original Paper

Master event based backazimuth estimation and its application to downhole microseismic monitoring

Xiao-Bo Meng [a], Hai-Chao Chen [b, *], Feng-Lin Niu [b, c], Yi-Jing Du [d]

[a] Department of Geophysics, Chengdu University of Technology, Chengdu, Sichuan, 610059, China
[b] Unconventional Petroleum Research Institute, and State Key Laboratory of Petroleum Resources and Prospecting, China University of Petroleum, Beijing, 102249, China
[c] Department of Earth, Environmental and Planetary Sciences, Rice University, Houston, TX, 77005, USA
[d] PetroChina Research Institute of Petroleum Exploration and Development, Beijing, 100083, China

ARTICLE INFO

Article history:
Received 9 March 2022
Received in revised form
12 April 2022
Accepted 6 June 2022
Available online 9 June 2022

Edited by Jie Hao

Keywords:
Hydraulic fracturing
Microseismic event
Back azimuth
Master event
Grid search
Covariance-matrix

ABSTRACT

Microseismic monitoring provides a valuable tool for evaluating the effectiveness of hydraulic fracturing operations. However, robust detection and accurate location of microseismic events are challenging due to the low signal to noise ratio (SNR) of their signals on seismograms. In a downhole monitoring setting, P-wave polarization direction measured from 3-component records is usually considered as the backazimuth of the microseismic event, i.e., the direction of the event. The direction and arrival time difference between the P and S waves is used to locate the seismic event. When SNR is low, an accurate estimate of event backazimuth becomes very challenging with the traditional covariance matrix method. Here we propose to employ a master event and use a grid search method to find the backazimuth of a target event that maximizes the dot product of the two backazimuthal vectors of the master and target events. We compared the backazimuths measured with the proposed grid-search and the conventional covariance-matrix methods using a large synthetic dataset. We found that the grid-search method yields more accurate backazimuth estimates from low SNR records when measurements are made at single geophone level. When array data are combined, the proposed method also has some advantage over the covariance-matrix method, especially when the number of geophones is low. We also applied the method to a microseismic dataset acquired by a hydraulic fracturing project at a shale play site in southwestern China and found that the relocated microseismic events tend to align along existing faults more tightly than those in the original catalog.

1. Introduction

Microseismic monitoring has been the primary technique for diagnosing hydraulic fracturing treatments over the past decade (Warpinski, 2009; Maxwell et al., 2010; Zhao et al., 2014). The basic idea of this technique is using the spatial distributions of the stimulated microseismic events to infer the geometry of the hydraulic fractures and calculate the stimulated reservoir volume (SRV) (e.g., Rutledge and Phillips, 2003; Lin and Ma, 2015; Wei et al., 2016; Heng et al., 2018). All the seismic events are important to characterize the newly created fracture network and to quantify the SRV. To obtain high signal to noise ratio (SNR) seismic data, a linear array is installed in a vertical or subvertical borehole near to the treatment well (Maxwell et al., 2010; Yan et al., 2013; Yang et al., 2014). With this acquisition geometry, P-wave propagation direction and S–P differential traveltimes are used in locating microseismic events (e.g., Oye and Roth, 2003; Jones et al., 2010; Yan et al., 2013; Mao et al., 2019). Earthquake location errors are generally related to inaccurate picks of P- and S-wave arrival times, uncertainties in estimates of P-wave propagation direction, and lack of detailed knowledge about the surrounding velocity structure (e.g., Zhang et al., 2013; Hirabayashi, 2016; Dai et al., 2016; Bray and White, 2020).

In an isotropic or weakly anisotropic medium, P-wave propagation direction is parallel or sub-parallel to its particle motion direction, therefore it can be estimated from three-component (3-C) seismic records. The linearly or elliptically polarized P-wave

* Corresponding author.
E-mail address: chchao@cup.edu.cn (H.-C. Chen).

https://doi.org/10.1016/j.petsci.2022.06.002

particle motion can be estimated from solving the eigenvalues and eigenvectors of the covariance matrix of multi-component records of the P-wave arrival (Bataille and Chiu, 1991; Niu and Li, 2011; Wang et al., 2016; Zhu et al., 2020). When the two horizontal records are used to construct a 2-D covariance matrix, then the major eigenvector (associated with the large eigenvalue) direction represents the backazimuthal direction, i.e., the backazimuthal vector. In the 3-D case, the eigenvector with the largest eigenvalue constitutes the propagation direction, including the backazimuthal direction and the incident angle in the horizontal and vertical planes, respectively. Hereinafter, we refer to this method as the covariance-matrix (CM) based method.

When noise is present in seismic records, the P-wave particle motion is always distorted from a linear or near-linear motion, leading to a deviation between the directions of wave propagation and the estimated eigenvector (Jurkevics, 1988; Bataille and Chiu, 1991). The deviation could be significant when SNR of the P-wave is low. Most of microseismic events induced by hydraulic fracturing are small ruptures, which radiate little seismic energy and register at stations as weak P-wave arrivals with a SNR < 1, whereas the accurate locations of these microseismic events are crucial for quantifying the spatial extent and complexity of hydraulic fractures (Williams-Stroud et al., 2013).

To reduce noise induced errors in the CM method, Jurkevics (1988) extended the single station-based technique to multiple 3-C sensors in an array configuration by averaging covariance matrices of different sensors. This CM stacking method can lead to $1/N$ reduction in the estimation variance where N is the number of the sensors. Meng et al. (2018) proposed an improved match and locate technique (iMLT), which incorporates the relative azimuth between the target event and template (master) event calculated with the CM method to the Match & Locate method (M&L) (Zhang and Wen, 2015), to improve event location with a vertical array. The relative azimuth between the target and master events is computed from their absolute backazimuth angles estimated with the single station CM method. Hence estimation error in relative azimuth could be worse than the large noise-induced errors in the absolute back azimuths due to error propagation. Li et al. (2013) proposed to employ cross-correlations of the two earthquakes to compute the differential backazimuth angle, which can be written as

$$\Delta\theta = \theta - \theta_0 = \tan^{-1}\frac{\int_{t_1}^{t_2}\{E_0(t)N(t) - N_0(t)E(t)\}\mathrm{d}t}{\int_{t_1}^{t_2}\{N_0(t)N(t) + E_0(t)E(t)\}\mathrm{d}t}, \tag{1}$$

where $(E_0(t),\ N_0(t))$ and $(E(t),\ N(t))$ are the east- and north-components of the master and target events, respectively. The P-wave arrivals of the two events are aligned and $[t_1, t_2]$ defines the time window of the P-wave arrivals. It should be noted that Eq. (1) was derived under the assumption of noise free data. However, we will show that it is valid even when uncorrelated (between different recording components and times) noise is present. Therefore, this method provides more accurate estimates of relative backazimuth when a single 3-C record is used. In this work, we propose a grid search method (GS) to estimate relative backazimuth angle between a pair of events by maximizing the dot product of their backazimuthal vectors.

The paper is organized as follows: we first describe the equations of CM and GS methods in a single station setting and a vertical array configuration in section 2. We then benchmark the two methods as well as the multi-component cross-correlation method (hereafter Li2013) using synthetic records of a large set of microseismic events in section 3. In section 4, we applied the proposed GS method to the microseismic dataset of Meng et al. (2018), which was acquired in a hydraulic fracturing project at a shale play site in southwestern China. Relocated seismicity with the GS measurements is compared to the results of Meng et al. (2018) and then further discussed.

2. Methodology

2.1. The covariance matrix method

As stated above, the CM method is based on the fact that propagation direction is parallel or sub-parallel to its particle motion direction when it traverses an isotropic or weakly anisotropic medium. A 3-D (e.g., Jurkevics, 1988) or 2-D (e.g., Niu and Li, 2011) covariance matrix is usually set up and the rectilinear particle motion direction is estimated through the eigenvector associated to the major eigenvalue. Here we employ the two horizontal components $(E(t), N(t))$ to define a 2-D covariance matrix:

$$\mathbf{C}_S = \begin{pmatrix} \int_{t_1}^{t_2} E(t)E(t)\mathrm{d}t & \int_{t_1}^{t_2} E(t)N(t)\mathrm{d}t \\ \int_{t_1}^{t_2} E(t)N(t)\mathrm{d}t & \int_{t_1}^{t_2} N(t)N(t)\mathrm{d}t \end{pmatrix} = \begin{pmatrix} c_{EE} & c_{EN} \\ c_{EN} & c_{NN} \end{pmatrix} \tag{2}$$

Likewise, $[t_1, t_2]$ defines the time window of P-wave. By solving the eigenproblem of the 2-D covariance matrix (Eq. (2)), the azimuth of the major eigenvector φ can be expressed as:

$$\varphi = \cot^{-1}\frac{c_{NN} - c_{EE} + \sqrt{(c_{NN} - c_{EE})^2 + 4c_{NE}^2}}{2c_{NE}}, \tag{3}$$

which is measured clockwise from the north. It can be shown that $\varphi = \theta$ or $\varphi = \theta \pm 180^\circ$ ($0^\circ \le \varphi, \theta < 360^\circ$, Fig. 1a) when noise is absent, where θ denotes the true backazimuth of the event. However, when noise is present, φ differs from θ and is given by

$$\begin{aligned} \cot\varphi &= \cot\theta + \frac{\sqrt{1 - 2h\cos 2\theta + h^2} - h - 1}{\sin 2\theta}; h \\ &= \frac{\sin^2\theta}{SNR_E^2 - 1} - \frac{\cos^2\theta}{SNR_N^2 - 1}, \end{aligned} \tag{4}$$

where SNR_E and SNR_N are the signal to noise ratios (SNR) of the E- and N-component of seismic recordings, respectively.

For the case of seismic array with a total number of N 3-C sensors, we defined the covariance matrix of the array by averaging the correlations of each sensor as (Jurkevics, 1988)

$$\mathbf{C}_A = \frac{1}{N}\begin{pmatrix} \sum_{i=1}^{N}\int_{t_{i1}}^{t_{i2}} \tilde{E}_i(t)\tilde{E}_i(t)\mathrm{d}t & \sum_{i=1}^{N}\int_{t_{i1}}^{t_{i2}} \tilde{E}_i(t)\tilde{N}_i(t)\mathrm{d}t \\ \sum_{i=1}^{N}\int_{t_{i1}}^{t_{i2}} \tilde{E}_i(t)\tilde{N}_i(t)\mathrm{d}t & \sum_{i=1}^{N}\int_{t_{i1}}^{t_{i2}} \tilde{N}_i(t)\tilde{N}_i(t)\mathrm{d}t \end{pmatrix} \tag{5}$$

where $\tilde{E}_i(t)$ and $\tilde{N}_i(t)$ indicate the E- and N-components of the i-th sensor normalized by $\int_{t_{i1}}^{t_{i2}}\{E_i(t) + N_i(t)\}^2\mathrm{d}t$, and $[t_{i1}, t_{i2}]$ is the P-wave time window of i-th sensor. Since all the records inside the array are from the same event, the P-wave time windows $[t_{i1}, t_{i2}]$ of

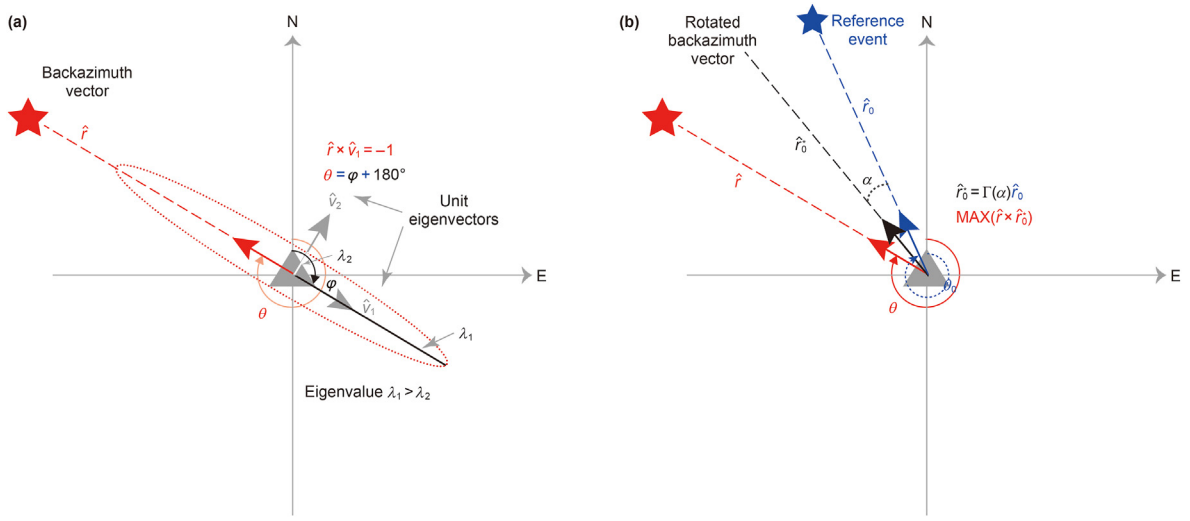

Fig. 1. Schematic diagram showing the CM method (a) and the GS method (b). The red star and grey triangle represent the target event and the receiver sensor, respectively. The red arrow represents the backazimuth vector $\hat{\mathbf{r}}$ of the target event with a backazimuth angle of θ. (a) The dashed ellipse represents the P-wave particle motion with a semi-major axis λ_1 in the direction $\hat{\mathbf{v}}_1$ (black arrow) and a semi-minor axis of λ_2 in the direction $\hat{\mathbf{v}}_2$ (grey arrow). φ is the azimuth of the $\hat{\mathbf{v}}_1$ measured clockwise from the north. (b) The blue star represents the master event, and the blue arrow represents its backazimuth vector $\hat{\mathbf{r}}_0$ with a backazimuth angle of θ_0. The vector $\hat{\mathbf{r}}_0^*$ (black arrow) is obtained by rotating $\hat{\mathbf{r}}_0$ with an angle of α.

different sensors are essentially the same if they are aligned. It is noted that $[t_{i1}, t_{i2}]$ can be taken differently among different sensors.

2.2. Master-event based grid searching method (GS)

Recent studies showed that template-matching techniques employing a set of well-located high-SNR master events is an effective way to detect and locate low-magnitude events that resemble to proximal master events (Song et al., 2010; Van der Elst et al., 2013; Skoumal et al., 2015; Bao and Eaton, 2016; Caffagni et al., 2016; Zhai et al., 2020; Zeng et al., 2021). Therefore, it is a reasonable approach to employ a master event and measure the relative backazimuth angle of a target event with respect to the master event. Fig. 1b presents the schematic diagram of our proposed GS method. Here, $\hat{\mathbf{r}}_0$ and $\hat{\mathbf{r}}$ are the backazimuth unit vectors of the master and target events, and their corresponding backazimuth angles are θ and θ_0, respectively. We rotate $\hat{\mathbf{r}}_0$ counterclockwise by an angle α to form a rotated unit vector $\hat{\mathbf{r}}_0^*$, and further compute the dot product between vector $\hat{\mathbf{r}}_0^*$ and $\hat{\mathbf{r}}$, which is denoted by $p_S(\alpha)$ and may be expressed in the form

$$p_S(\alpha) = \left[\int_{t_1}^{t_2} \{E_0(t)N(t) - N_0(t)E(t)\}\mathrm{d}t\right]\sin\alpha + \left[\int_{t_1}^{t_2} \{N_0(t)N(t) + E_0(t)E(t)\}\mathrm{d}t\right]\cos\alpha, \tag{6}$$

where $(E_0(t), N_0(t))$ and $(E(t), N(t))$ are the E- and N- components of the master and target events, respectively. It should be noted that in case of uncorrelated noise among different time windows, the cross-event correlations are expected to be less sensitive to noise than the single-event correlations, leading to a more robust estimate of α with single station records under noisy condition. It can also be seen that $p_S(\alpha)$ reaches to the maximum when $\mathrm{d}p_S(\alpha)/\mathrm{d}\alpha = 0$, i.e.,

$$\tan(\alpha) = \tan(\theta - \theta_0) = \frac{\int_{t_1}^{t_2} \{E_0(t)N(t) - N_0(t)E(t)\}\mathrm{d}t}{\int_{t_1}^{t_2} \{N_0(t)N(t) + E_0(t)E(t)\}\mathrm{d}t}, \tag{7}$$

Eq. (7) is exactly the same as Eq. (1) proposed by Li et al. (2013). We should emphasize that Eq. (1) was derived under the noise-free condition, and we showed that it could be a good approximation even low SNR records were used. In real data, noise is unlikely perfectly random, therefore the ratio of cross-event correlations in Eq. (7) could be off the maximum $p_S(\alpha)$. We thus conduct a grid search of the optimum α that has the maximum $p_S(\alpha)$.

Similar to the CM method, we can also define a dot product for a vertical array with N 3-C sensors:

$$p_A(\alpha) = \left[\frac{1}{N}\sum_{i=1}^{N}\int_{t_{i1}}^{t_{i2}} \left\{\tilde{E}_{0i}(t)\tilde{N}_i(t) - \tilde{N}_{0i}(t)\tilde{E}_i(t)\right\}\mathrm{d}t\right]\sin\alpha + \left[\frac{1}{N}\sum_{i=1}^{N}\int_{t_{i1}}^{t_{i2}} \left\{\tilde{E}_{0i}(t)\tilde{E}_i(t) + \tilde{N}_{0i}(t)\tilde{N}_i(t)\right\}\mathrm{d}t\right]\cos\alpha \tag{8}$$

where $(\tilde{E}_{0i}(t), \tilde{N}_{0i}(t))$ and $(\tilde{E}_i(t), \tilde{N}_i(t))$ represent the normalized E- and N-component records of the master and target events recorded by the i-th sensor. The P-wave arrivals of the two events are aligned and $[t_{i1}, t_{i2}]$ defines the time window of the P-wave arrivals at the i-th sensor. As mentioned above, this window could be the same among all the sensors. We also employ a grid search of α to find the maximum $p_A(\alpha)$.

Li et al. (2013) did not mention how to integrate an array data to compute the relative backazimuth angle. Here we simply use the mean of all the single station measurements to compute averaged estimate across the array, given by

$$\Delta\theta_A = \frac{1}{N}\sum_{i=1}^{N}\Delta\theta_i, \tag{9}$$

where $\Delta\theta_i$ is defined by Eq. (1).

3. Synthetic tests

To evaluate the accuracy of the three methods, CM, GS, and Li2013, we first apply them to 4 synthetic datasets and each one is composed of one master event and 200 target events, which are recorded by a vertical array with 20 3-C sensors. The source-receiver geometry is based on a field microseismic experiment in SW China (Meng et al., 2018, hereinafter referred to as the FEM18 dataset). More specifically, the 20 geophones are deployed at a depth from ~2115 m to ~2400 m with a sensor spacing of 15 m, and the induced microearthquakes occur at ~2700 m with lateral distances of ~500 m from the geophone array. From the FEM18 dataset, we first selected one microseismic event with a high SNR as the master event. The event was one of the 10 template events used in the iMLT analysis, and its seismograms at the 20 geophones were aligned at the onset of the Pwaves, which was set to time zero. We used the same master event among the 4 datasets. We assumed that the P-wave arrival windows of the target events were measured from the iMLT analysis and therefore were known. For each target event, its seismograms at the 20 geophones were also aligned at the onset of the P waves. It is worth noting that computing P-wave traveltimes was not required, thus a velocity model was not needed in our synthetic calculation.

To synthesize seismograms of the 200 target events, we first randomly generated their source locations (hypocenters), which are located within 150 m from the master event and with a relative backazimuth angle between -20° and 20°. We assumed that the P-wave propagates along the straight line between each target event and geophone and projected the P-wave motion vectors to the Z-, N-, and E-components. For the datasets 1 and 2, we employed the P waveforms of the master event as the source wavelets, and for the datasets 3 and 4, we used the P waveforms of another template event of the FEM18 dataset as the source wavelets. We further randomly took 200 noise windows which were also taken from the FEM18 dataset and summed each noise window with the P-wave arrivals. By properly scaling the noise and P-wave amplitude, we were able to obtain 3-C synthetic seismograms of the 200 target events in each dataset with the desired SNR. The noise window was taken several times longer than the P-wave signal window. To calculate SNR, we took a noise window prior to P-wave with a duration twice long as the P-wave window and computed the average energy of the noise and P-wave windows. The SNR is defined as the square root of the average energy ratio between the P-wave and noise windows. The first dataset was meant for large-magnitude events, which has an average SNR of 10.6 and standard deviation of 4.9 from the N-component recordings (Table 1). An example of the E- and N-component records is shown in Fig. 2a.

We used a window length of 0.015 s that encloses the whole P-wave signal (see the grey shaded window in Fig. 2a) to make backazimuth measurements. Fig. 2b shows an example of the GS measurement, i.e., a single station dot product, $p_S(\alpha)$, as a function of the absolute backazimuth $(\theta_0 + \alpha)$. The angle corresponding to the maximum $p_S(\alpha)$ is the measured backazimuth by the GS method (red line in Fig. 2b). Fig. 2c shows an example of particle motion of the P-wave window (grey shaded in Fig. 2a) at one of the 20 stations. The blue line indicates the major eigenvector direction while the black line represents the true back azimuth direction. For each event we made 20 backazimuth measurements across the whole array with the GS method, and we further computed their deviations from the true backazimuth. We applied this procedure to all the 200 events, and Fig. 2d shows the histogram of the 20×200 deviations by the GS method. For comparison, we also plotted the histogram of the 20×200 measurements with the CM method in Fig. 2e. In general, both methods yield very accurate measurements with a mean close to 0.0° and a standard deviation of less than 1.5° even with the single-station-based approach. When the two methods were implemented in the array configuration, the estimates are close to the true backazimuths of the 200 events. A zero mean value is obtained by both methods and a standard deviation of 0.3° and 0.1° is achieved by the CM and GS methods, respectively. For further comparison, we also made similar measurements with the Li2013 method, and the results are listed in the first line of Table 1. It is obvious that the measurement accuracy of the three methods is rather similar when they are applied to high SNR data.

The second dataset was designed for low magnitude microseismic events. The average SNR is ~1.4 (Table 1). An example of the E- and N-component records, the GS and CM single-station measurements, and the histograms of the 20×200 measurements of the two methods are shown in Fig. 2f-j. The array-based measurements as well as estimates from the Li2013 method are all listed in Table 1. In general, the single-station measurements from GS and Li2013 are comparable, which are approximately one time better than those derived from the CM method. For the array-based measurements, the GS produces the smallest mean value and standard deviation (second line of Table 1).

We have assumed that the 200 target events have the same source wavelets as the master event in the above two datasets. Next, we would like to test whether this assumption could affect the results of the proposed method, as cross-event correlations are used in computing the dot product of the backazimuth vectors. To do so, we employed another template event, which has a source wavelet distinctly different from the master event, to generate two sets of 200 microseismic events with high and low SNR values, respectively. Fig. 3 shows 7 examples of 3-C waveforms of the P-wave arrivals with blue solid and red dotted lines indicating the target and master events, respectively. The average cross-correlation coefficient of the two events is 0.55. We employed the same procedure in generating the 200 target events and their corresponding 3-C synthetic seismograms.

Similar to dataset 1, dataset 3 was designed for large-magnitude events with high SNR, the measurement results of the three methods based on single-station and array configuration are listed in the third lines of Table 1. As expected, the three methods work well in estimating the backazimuth angles of all the events with a standard deviation of ~1.8°–2.5° for the single-station based measurements and ~0.2°–0.4° for the array estimates. We notice that both the mean and standard deviation values are slightly larger

Table 1
List of mean and standard deviation and backazimuth residuals measured by the three methods.

Dataset	SNR			CM		GS		Li2013	
	E	N	Z	S, °[a]	A, °[a]	S, °[a]	A, °[a]	S, °[a]	A, °[a]
1	2.7 ± 1.0	10.6 ± 4.9	14.9 ± 4.1	0.0 ± 1.3	0.0 ± 0.3	−0.1 ± 1.0	0.0 ± 0.1	−0.1 ± 1.0	−0.1 ± 0.3
2	1.0 ± 0.1	1.5 ± 0.4	1.8 ± 0.4	0.3 ± 18.3	−0.6 ± 2.8	−0.3 ± 11.1	0.0 ± 1.4	−0.7 ± 11.1	−0.0 ± 3.1
3	2.6 ± 1.0	7.9 ± 3.5	11.9 ± 2.8	0.2 ± 1.8	0.2 ± 0.4	1.6 ± 2.5	0.4 ± 0.2	1.0 ± 2.4	1.0 ± 0.4
4	1.0 ± 0.1	1.3 ± 0.3	1.6 ± 0.3	0.6 ± 28.6	−0.1 ± 4.1	1.3 ± 15.8	0.7 ± 2.5	1.0 ± 17.3	1.0 ± 3.9

[a] S: single station; A: a hypothetical array with 20 3-C geophones.

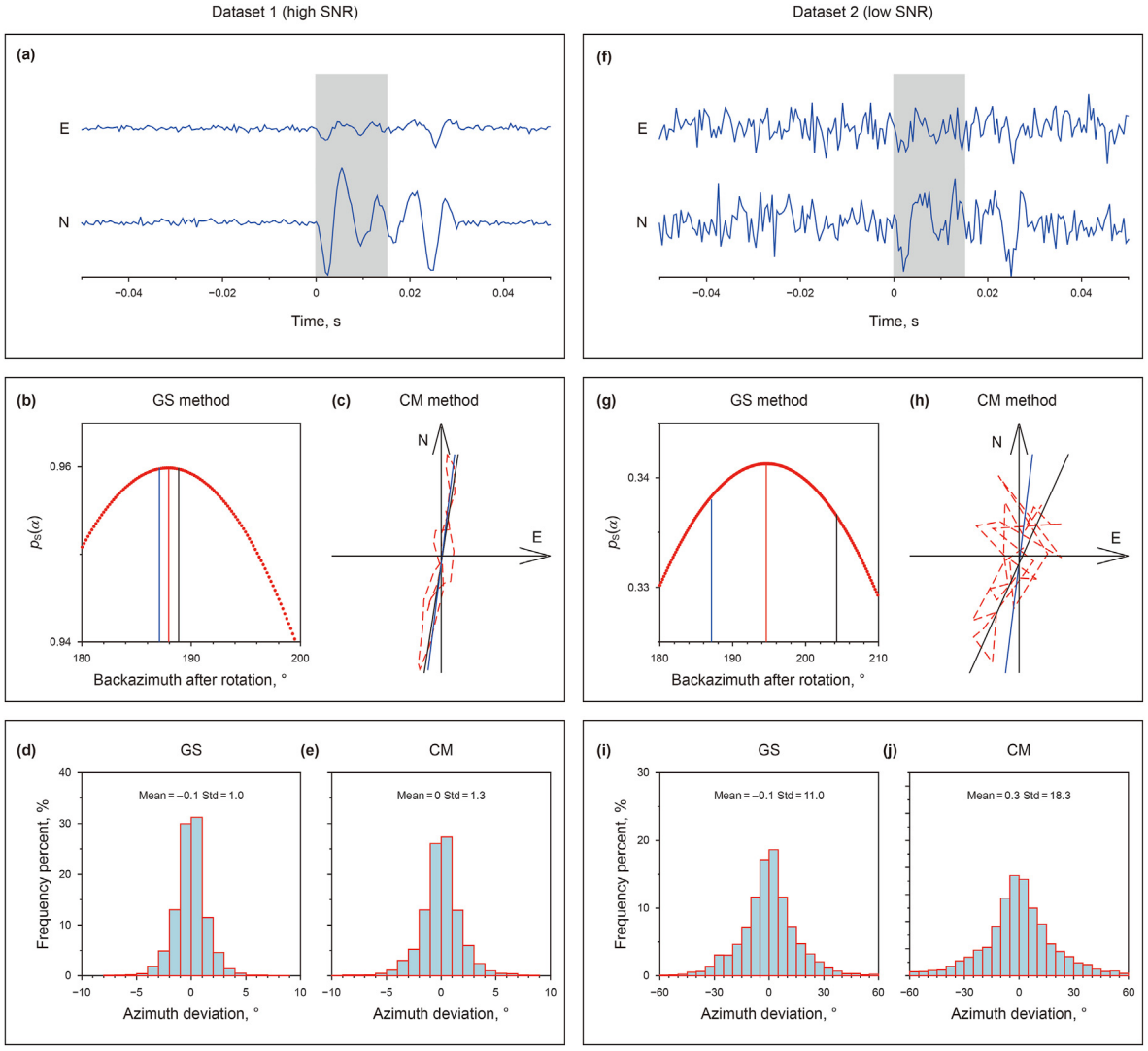

Fig. 2. (a) An example of the E- and N-component records of the dataset 1 with a high SNR. Grey shaded area indicate the P-wave time window used in computing the dot product, i.e., $p_S(\alpha)$. (b) $p_S(\alpha)$ is plotted as a function of the absolute backazimuth of the target event. Vertical red and black lines indicate the measured backazimuth with the GS method and true backazimuth of the target event. For comparison, measurement with the CM method is shown by the vertical blue line. (c) Particle motion of the P-wave is shown in red dashed line. Blue and black straight lines indicate the CM measurement and the true backazimuth of the target event. (d) and (e) are histograms of deviations of GS and CM single station measurements from the true backazimuths of the 200 microseismic events. (f)–(j) are the same as (a)–(e) except for the synthetic dataset, which is the low SNR dataset 2.

than those of dataset 1, implying that waveform similarity between the master and the target events does have a slight influence on the measurement accuracy. However, it is also true that dataset 3 has a slightly lower average SNR than dataset 1, which may partly contribute to the large mean and standard deviation values of dataset 3. The source wavelets of the 200 microseismic events in dataset 4 are similar to those in dataset 3, which are different from the master event waveform. The average SNR and the measurements of the three methods are listed in the fourth line of Table 1. Compared to the measurements derived from dataset 2, the mean and standard deviation values of the dataset 4 are both slightly higher.

As listed in Table 1, among the three array-based measurements, our proposed GS method yields the smallest standard deviation values in all the four datasets. To further show how the number of 3-C sensors in an array affects the measurements of the three methods, we varied the number of stations in an array from 1 to 20 and used the two low SNR datasets (datasets 2 and 4) in the investigation. Fig. 4a and b shows the standard deviations measured from arrays with different number of stations from the datasets 2 and 4, respectively. It should be noted that we took the stations sequentially from the top to the bottom in configuring hypothetic arrays with station number from 1 to 20. Since stations at the top are further away from the microseismicity, their seismic records generally have lower SNR as compared to those in the bottom of the vertical array. Therefore, measurements with the hypothetic arrays with a small number of top stations yield higher standard deviations than single-station measurements, which were averaged over the 20 stations. The standard deviations of the three measurements all decrease with increasing station number, and among the three the GS method gives the best measurements. When station number is small, the advantage of the GS method becomes significant.

4. Field data application

We have also applied the proposed GS method to a filed dataset recorded by a 20-level geophone array installed in a deep

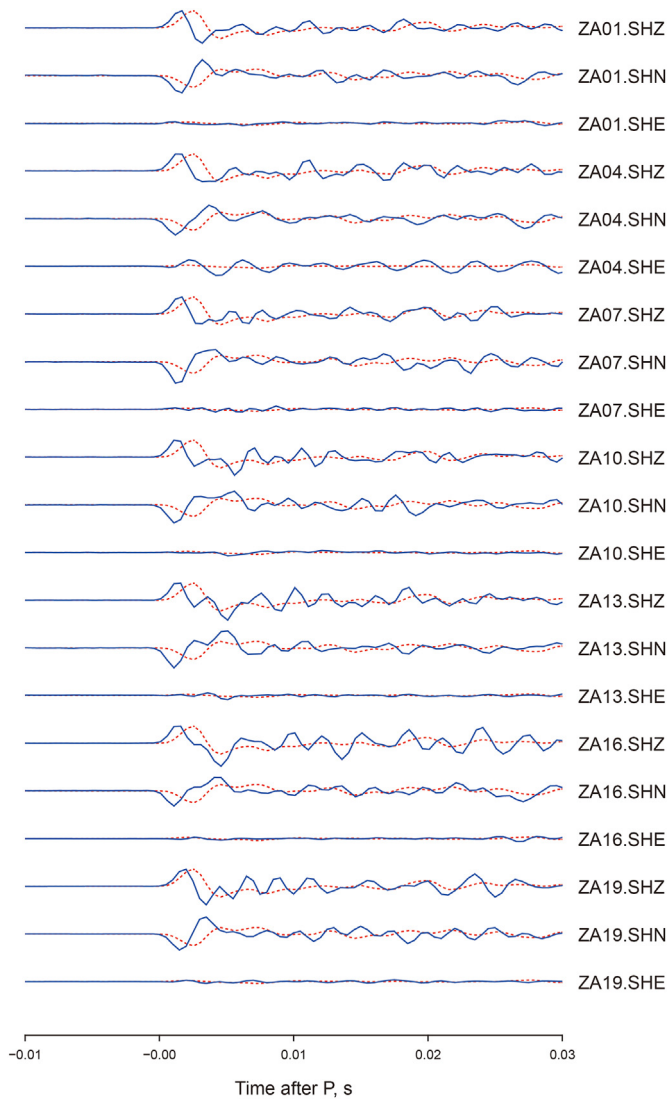

Fig. 3. Seven examples of 3-C records of the P waveforms of the master event (red dotted lines) and the target events (blue solid line) used in generating datasets 3 and 4. The waveforms of master event were also used in generating the target events of datasets 1 and 2.

monitoring well during a hydraulic fracturing operation conduced within the Sichuan Basin in southwestern China. We first calculated the orientation of each sensor using signals of perforation shots fired before hydraulic injection, and then rotated the recorded data to Z-N-E coordinate. Meng et al. (2018) applied the iMLT method to the dataset and detected a total of 326 events. For each event, they employed a relative location method using the relative back-azimuth angles and S–P travel times with respective to a master event to locate the earthquakes. The left panel of Fig. 5 shows the 3-D locations of the 326 events (Meng et al., 2018). The relative backazimuth of each event was computed using the single-station-based CM method.

In this study, we recalculated the relative backazimuth angle of each event using the array-based GS method. We then relocated the 326 events by incorporating the GS measurements into the iMLT location engine. The right panel of Fig. 5 shows the relocation results. Apparently, the distribution of the events in the red ellipse is more tightly clustered after relocation. The average Euclidean distance of the events in the ellipse to the cluster center is 39.4 m, smaller than the 46.4 m computed from the original catalog. In addition, the geometry of a potential fault is more clearly delineated (right panel of Fig. 5), which strengths the speculation of Chen et al. (2018) that these events are likely nested on a critically stressed fault, which was reactivated by the hydraulic fracturing operations.

5. Conclusions

Recent studies suggest that relative location techniques provide better constraints on spatial distribution of microseismicity. These techniques usually involve measurements of relative seismic properties with respect to a master event, such as relative traveltimes and relative backazimuth angles. We proposed a grid search-based method to determine the relative angle between the target and master events by maximizing the dot product of the backazimuth vectors of the two events. We showed analytically that the GS method is less sensitive to uncorrelated noise than the traditional CM method. When noise is completely uncorrelated in time, then our method becomes equivalent to Li2013. We investigated the accuracy of our GS method using large synthetic data, which incorporate real noise extracted from a field experiment. We found that the GS method has a noticeable advantage over the existing CM and Li2013 methods when applied to single station

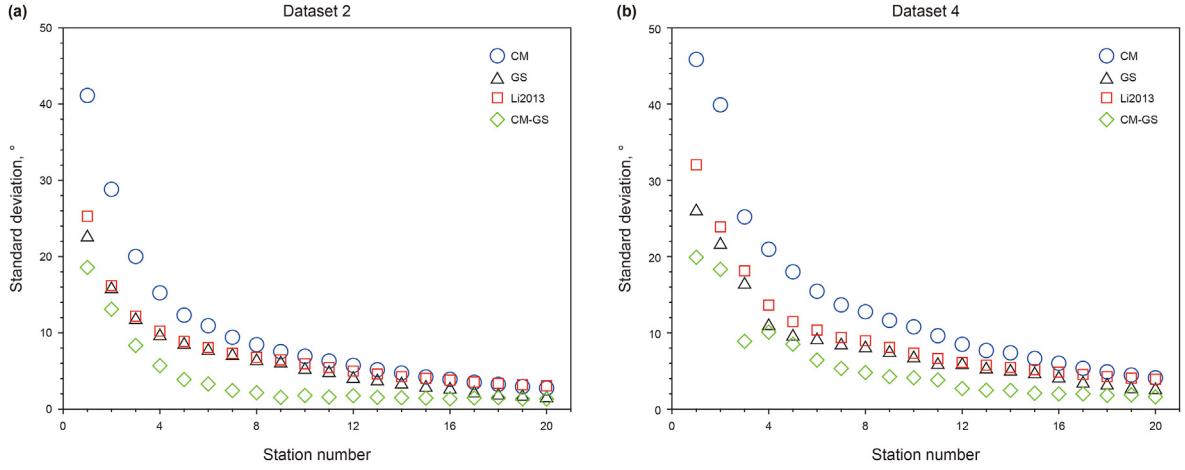

Fig. 4. The standard deviation of the backazimuth residuals (i.e., estimated backazimuth minus true backazimuth) is plotted as a function station number in an array. The residuals are computed with the estimates from the CM, GS, Li2013 methods using the low SNR dataset 2 (a) and dataset 4 (b).

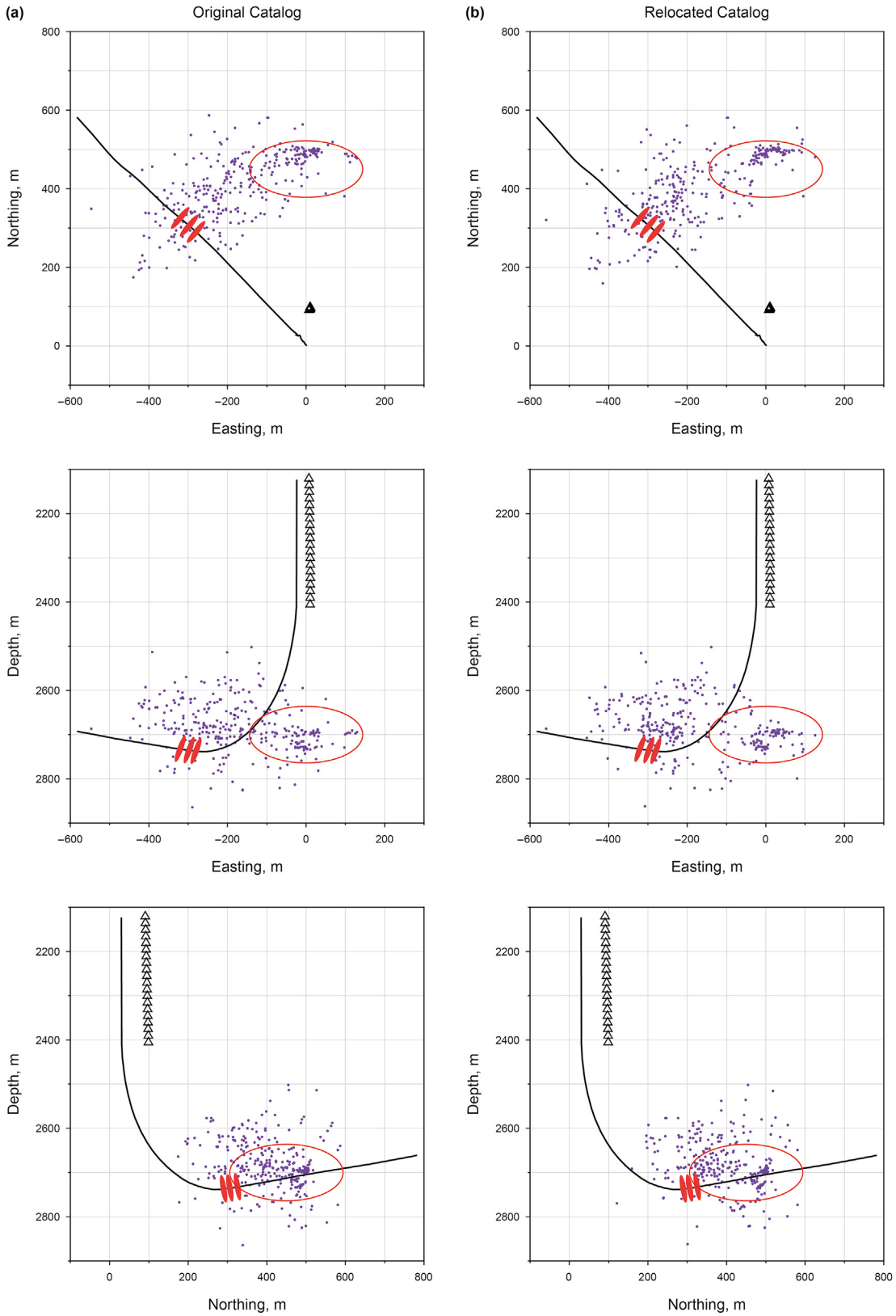

Fig. 5. Spatial distribution of the 326 microseismic events (blue dots) in the two vertical and one horizontal planes. (a) Original locations from Meng et al. (2018). (b) Relocated catalog with GS estimates of event backazimuth. The thick solid black line shows the trajectory of the treatment well. Open black triangles represent the 3-C sensors in a monitoring well. Three red ellipsoids indicate locations of three perforation shots.

data. In case of making a single estimate by a station array, our method still shows superior performance to the CM method, and this advantage becomes more significant when the number of sensors in the vertical array is small. Application the GS method to field data also suggests that it can lead to a better location of microseismicity.

Acknowledgments

We would like to thank Sichuan Geophysical Company of China National Petroleum Company (CNPC) (http://ccde.cnpc.com.cn/) for providing the field data set and permission to publish this work. We are also grateful for the constructive comments and suggestions from the associate editor and two anonymous reviewers, which significantly improved the quality of this paper. This study was supported by the National Natural Science Foundation of China (Grants No. 41630209 and 41974045).

References

Bao, X.W., Eaton, D.W., 2016. Fault activation by hydraulic fracturing in western Canada. Science 354 (6318), 1406–1409. https://doi.org/10.1126/science.aag2583.

Bataille, K., Chiu, J.M., 1991. Polarization analysis of high-frequency, three-component seismic data. Bull. Seismol. Soc. Am. 81 (2), 622–642. https://doi.org/10.1785/BSSA0810020622.

Bray, M., White, I., 2020. Understanding acquisition and processing error in microseismic data: an example from Pouce Coupe Field, Canada. Geophys. Prospect. 68 (3), 815–829. https://doi.org/10.1111/1365-2478.12887.

Caffagni, E., Eaton, D.W., Jones, J.P., et al., 2016. Detection and analysis of microseismic events using a Matched Filtering Algorithm (MFA). Geophys. J. Int. 206 (1), 644–658. https://doi.org/10.1093/gji/ggw168.

Chen, H.C., Meng, X.B., Niu, F.L., et al., 2018. Microseismic monitoring of stimulating shale gas reservoir in SW China: 2. Spatial clustering controlled by the preexisting faults and fractures. J. Geophys. Res. Solid Earth 123 (2), 1659–1672. https://doi.org/10.1002/2017JB014491.

Dai, F., Guo, L., Xu, N.W., et al., 2016. Improvement of microseismic location based on an anisotropic velocity model. Chin. J. Geophys. 59 (9), 3291–3301, 0.6038/cjg20160914. (in Chinese).

Heng, F., Wang, G., Liu, B., et al., 2018. Hydraulic fracturing with different cluster spacing based on microseismic monitoring. Oil Geophys. Prospect. 53 (2), 137–142. https://doi.org/10.13810/j.cnki.issn.1000-7210.2018.S2.021 (in Chinese).

Hirabayashi, N., 2016. Real-time event location using model-based estimation of arrival times and back azimuths of seismic phases. Geophysics 81 (2), KS25–KS40. https://doi.org/10.1190/geo2014-0357.1.

Jones, G.A., Raymer, D., Chambers, K., et al., 2010. Improved microseismic event location by inclusion of a priori dip particle motion: a case study from Ekofisk. Geophys. Prospect. 58 (5), 727–737. https://doi.org/10.1111/j.1365-2478.2010.00873.x.

Jurkevics, A., 1988. Polarization analysis of three-component array data. Bull. Seismol. Soc. Am. 78 (5), 1725–1743. https://doi.org/10.1785/BSSA0780051725.

Li, J.L., Zhang, H.J., Rodi, W.L., et al., 2013. Joint microseismic location and anisotropic tomography using differential arrival times and differential backazimuths. Geophys. J. Int. 195 (3), 1917–1931. https://doi.org/10.1093/gji/ggt358.

Lin, A., Ma, J., 2015. Stimulated-rock characteristics and behavior in multistage hydraulic-fracturing treatment. SPE J. 20 (4), 784–789. https://doi.org/10.2118/167716-PA.

Mao, Q.H., Wang, P., Azeem, T., 2019. Microseismic event location using an improved global grid search and its extended method in a downhole monitoring system. J. Geophys. Eng. 16 (1), 159–174. https://doi.org/10.1093/jge/gxy014.

Maxwell, S.C., Rutledge, J., Jones, R., et al., 2010. Petroleum reservoir characterization using downhole microseismic monitoring. Geophysics 75 (5), 75A129–75A137. https://doi.org/10.1190/1.3477966.

Meng, X.B., Chen, H.C., Niu, F.L., et al., 2018. Microseismic monitoring of stimulating shale gas reservoir in SW China: 1. An improved matching and locating technique for downhole monitoring. J. Geophys. Res. Solid Earth 123 (2), 1643–1658. https://doi.org/10.1002/2017JB014488.

Niu, F.L., Li, J., 2011. Component azimuths of the CEArray stations estimated from P-wave particle motion. Earthq. Sci. 24 (1), 3–13. https://doi.org/10.1007/s11589-011-0764-8.

Oye, V., Roth, M., 2003. Automated seismic event location for hydrocarbon reservoirs. Comput. Geosci. 29 (7), 851–863. https://doi.org/10.1016/S0098-3004(03)00088-8.

Rutledge, J.T., Phillips, W.S., 2003. Hydraulic stimulation of natural fractures as revealed by induced microearthquakes, Carthage Cotton Valley gas field, east Texas. Geophysics 68 (2), 441–452. https://doi.org/10.1190/1.1567214.

Skoumal, R.J., Brudzinski, M.R., Currie, B.S., 2015. Distinguishing induced seismicity from natural seismicity in Ohio: demonstrating the utility of waveform template matching. J. Geophys. Res. Solid Earth 120, 6284–6296. https://doi.org/10.1002/2015JB012265.

Song, F.X., Kuleli, H.S., Toksöz, M.N., et al., 2010. An improved method for hydrofracture-induced microseismic event detection and phase picking. Geophysics 75 (6), A47–A52. https://doi.org/10.1190/1.3484716.

Van der Elst, N.J., Savage, H.M., Keranen, K.M., et al., 2013. Enhanced remote earthquake triggering at fluid-injection sites in the midwestern United States. Science 341 (6142), 164–167. https://doi.org/10.1126/science.1238948.

Wang, X., Chen, Q.F., Li, J., et al., 2016. Seismic sensor misorientation measurement using P-wave particle motion: an application to the NECsaids array. Seismol Res. Lett. 87 (4), 901–911. https://doi.org/10.1785/0220160005.

Warpinski, N., 2009. Microseismic monitoring: inside and out. J. Petrol. Technol. 61 (11), 80–85. https://doi.org/10.2118/118537-JPT.

Wei, M.Q., Duan, Y.G., F, Q.T., et al., 2016. Production decline analysis for a multi-fractured horizontal well considering elliptical reservoir stimulated volumes in shale gas reservoirs. J. Geophys. Eng. 13 (3), 354–365. https://doi.org/10.1088/1742-2132/13/3/354.

Williams-Stroud, S., Ozgen, C., Billingsley, R.L., 2013. Microseismicity-constrained discrete fracture network models for stimulated reservoir simulation. Geophysics 78 (1), B37–B47. https://doi.org/10.1190/geo2011-0061.1.

Yan, Y.X., Zhang, Y.H., Chen, X., et al., 2013. The application of microseismic technology in fracture monitoring. Earth Sci. Front. 20 (3), 270–274. CNKI:SUN:DXQY.0.2013-03-033. (in Chinese).

Yang, B.X., Yang, Y.T., Li, R., et al., 2014. Application of downhole microseismic fracture monitoring technology in staged fracturing of horizontal well. Drill. Prod. Technol. 37 (4), 48–50. https://doi.org/10.3969/J.ISSN.1006-768X.2014.04.15 (in Chinese).

Zeng, Q., Chu, R.S., Sheng, M.H., et al., 2021. Preliminary study on microseismic signals of danba suopo landslide in sichuan province. Earthq. Res. China 37 (2), 300–308. https://doi.org/10.3969/j.issn.1001-4683.2021.02.005 (in Chinese).

Zhai, S., Yu, Z.C., Tan, Y.Y., et al., 2020. Microseismic monitoring events classification based on waveform clustering analysis and application. Acta Sci. Nauralium Univ. Pekin. 56 (3), 406–416. https://doi.org/10.13209/j.0479-8023.2020.01.

Zhang, M., Wen, L.X., 2015. An effective method for small event detection: match and locate (M&L). Geophys. J. Int. 200 (3), 1523–1537. https://doi.org/10.1093/gji/ggu466.

Zhang, X.L., Zhang, F., Li, X.Y., et al., 2013. The influence of hydraulic fracturing on velocity and microseismic location. Chin. J. Geophys. 56 (10), 3552–3560. https://doi.org/10.6038/cjg201303 (in Chinese).

Zhao, B.X., Wang, Z.G., Liu, R., et al., 2014. Review of Microseismic monitoring technology research. Prog. Geophys. 29 (4), 1882–1888. https://doi.org/10.6038/pg20140454 (in Chinese).

Zhu, G.H., Yang, H.F., Lin, J., et al., 2020. Determining the orientation of ocean-bottom seismometers on the seafloor and correcting for polarity flipping via polarization analysis and waveform modeling. Seismol Res. Lett. 91 (2A), 814–825. https://doi.org/10.1785/0220190239.